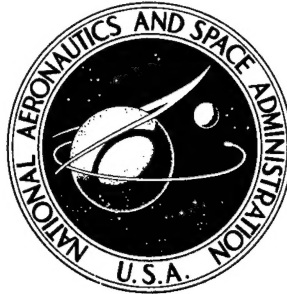


72484

NASA TECHNICAL NOTE



NASA TN D-4526

NASA TN D-4526

# AMPTIAC

DISTRIBUTION STATEMENT A:  
Approved for Public Release -  
Distribution Unlimited

## (THE USE OF THE ELECTRON PROBE MICROANALYZER IN MATERIALS RESEARCH AND DEVELOPMENT)

*by Lawrence Kobren*

*Goddard Space Flight Center  
Greenbelt, Md.*

20020916 071

B072484

NASA TN D-4526

THE USE OF THE ELECTRON PROBE MICROANALYZER  
IN MATERIALS RESEARCH AND DEVELOPMENT

By Lawrence Kobren

Goddard Space Flight Center  
Greenbelt, Md.

Copies Furnished to DTIC  
Reproduced From  
Bound Original

Reproduced From  
Best Available Copy

NATIONAL AERONAUTICS AND SPACE ADMINISTRATION

---

For sale by the Clearinghouse for Federal Scientific and Technical Information  
Springfield, Virginia 22151 - CFSTI price \$3.00

## ABSTRACT

*from p. 1*

The electron probe microanalyzer, a versatile tool for the analysis of areas as small as one micron in diameter, has been used at Goddard Space Flight Center in applications ranging from materials research to analysis of failures in mechanical parts. Methods of using the probe and representative results obtained are illustrated by several examples that include bonding of thermoelectric materials, alloy development, and analysis of materials failures.

*end*

## CONTENTS

	<u>Page</u>
Abstract . . . . .	ii
INTRODUCTION . . . . .	1
DESCRIPTION OF THE INSTRUMENT . . . . .	1
THERMOELECTRIC BONDING STUDIES . . . . .	3
PbTe-W DIFFUSION BOND . . . . .	5
SiGe-W DIFFUSION BOND . . . . .	6
STRENGTHENING OF PbTe . . . . .	7
FAILURE ANALYSIS OF H <sub>2</sub> O <sub>2</sub> STORAGE BOTTLE . . . . .	9
ALLOY DEVELOPMENT . . . . .	11
Ruthenium vs Zinc Reactions . . . . .	11
Rhodium-Zinc . . . . .	13
Rhenium Alloys . . . . .	14
Magnesium-Yttrium-Aluminum Alloys . . . . .	14
FRICITION AND WEAR . . . . .	17
FAILURE OF NIMBUS SEPARATION SPRINGS . . . . .	21
CONCLUDING COMMENT . . . . .	22
References . . . . .	22

# THE USE OF THE ELECTRON PROBE MICROANALYZER IN MATERIALS RESEARCH AND DEVELOPMENT

by  
Lawrence Kobren  
*Goddard Space Flight Center*

## INTRODUCTION

For several years Goddard Space Flight Center has had at its disposal a unique tool, the electron microprobe X-ray analyzer (EMX), that has been used to analyze numerous materials ranging from metals to semiconductors. The ability to perform elemental analyses, both qualitatively and quantitatively, of a volume of a few cubic microns (1 micron = 0.001 mm) is a unique capability of the instrument. The <sup>A11</sup>analysis can be performed *in situ* and nondestructively. Since such a small volume can be examined, analysis of individual <sup>A11</sup>grains, grain boundaries, inclusions, etc. can be performed easily. The sensitivity (limit of detectability) of this method of analysis ranges from one part in  $10^5$  (0.001 percent) to one part in  $10^3$  (0.1 percent), depending on the element of interest, the matrix, and the size of the electron beam. The relative accuracy is 1 to 2 percent if the concentration of the element is greater than a few percent, and if adequate standards are available. The purpose of this report is to illustrate the versatility of the electron probe and to summarize some of the materials investigations conducted by the Materials Research and Development Branch which have relied on the probe as a major part of the analysis.

## DESCRIPTION OF THE INSTRUMENT

Basically the operation of the EMX (Figure 1) uses a fine beam of electrons which is focused by electromagnetic lenses on a spot approximately 1 micron in diameter at the surface of the specimen. The specimen is suitably held in a metallurgical mount and must be highly polished, though not etched. An optical microscope is incorporated in the instrument to permit visual observation of the specimen during analysis. X-rays, characteristic of the elements present in the sample, are produced as a

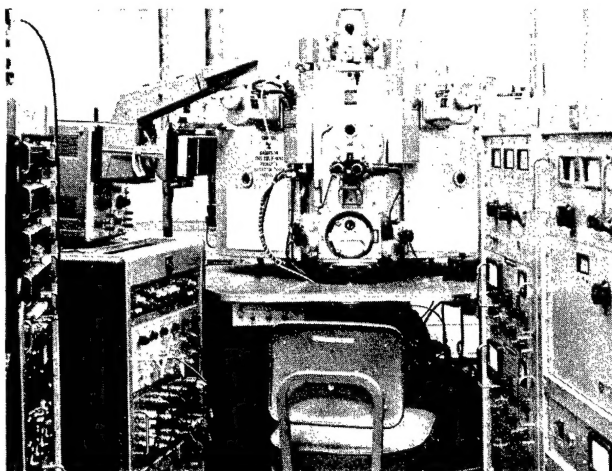


Figure 1—The electron microprobe X-ray analyzer.

result of the electron bombardment and are sorted by one or more of the three spectrometers within the instrument. These spectrometers contain five different analyzing crystals that detect X-rays in the wavelength region from 1 to 68.9Å. This permits analysis of all elements above atomic number 5 (boron). In addition to the channels of the three spectrometers, others are available to monitor backscattered electron and sample current signals. The number of electrons backscattered from the specimen is a direct function of the atomic number of the element. The sample current, a measure of the number of electrons collected, is an inverse function of the atomic number; that is, lighter elements will give a higher sample current than will heavy elements for the same number of electrons hitting the surface. The signals from both of these modes of operation can be fed to one of several readout displays, including a recorder, a scaler, or an oscilloscope. Spectral line scanning can be done manually or automatically, with the dials on the spectrometer calibrated in angstrom units for easy readout.

The specimen within the instrument can be moved along two axes manually or moved under the electron beam at a constant rate of 8 or 96 microns per minute. If desired, the specimen also can be automatically moved in incremental steps varying from 1 to 10 microns per step. The X-ray signal from one or all of the spectrometers can be sent simultaneously to a 3-pen recorder so that X-ray intensity can be plotted as a function of probe position on the specimen.

An electron beam scanning system is incorporated into the EMX. In this mode of operation, the electron beam moves vertically and horizontally across the surface of the specimen. This is accomplished by means of four electrostatic deflection plates surrounding the electron beam. The plate voltages which control beam deflection are controlled by two time-base units of an oscilloscope. The amplified signal from the X-ray detection system is fed to the oscilloscope for intensity modulation and becomes a function of the beam position. If, for example, a spectrometer is set to a desired wavelength, i.e., representative of some particular element, and the incoming X-ray signal is sent to the oscilloscope during the scanning mode of operation, a two-dimensional pattern of the specimen is obtained on the screen, thus presenting the distribution of that element within the specimen. Similar results can be obtained by sending the backscattered signal or sample current signal to the oscilloscope. The backscattered and sample current displays give a general indication of the distribution of the elements as well as holes in the specimen surface. The distribution of the elements presented by this display is caused by the difference in atomic number of the elements. Magnification of the area being examined can be increased progressively by reducing both the X- and Y-axis deflections of the probe by 1/2, 1/4, 1/8, 1/16, and 1/32 while the area viewed on the oscilloscope (8 cm × 8 cm) remains constant.

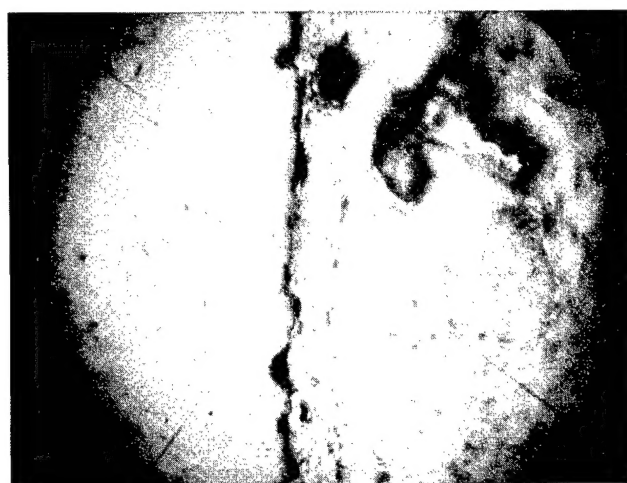
Quantitative analysis can be performed by measuring the intensities of X-rays emitted by the sample and comparing them to intensities from materials of known composition. As a first approximation, Castaing (Reference 1) proposed  $I/I_0 = C_a$ , where  $I$  is the X-ray intensity generated in the sample,  $I_0$  is the intensity measured in the pure element, and  $C_a$  is the concentration of the element "a" in the sample. X-rays generated within the sample are attenuated by their passage through it; therefore, the intensities measured by the detectors must be corrected for absorption effects, fluorescence effects, and atomic number effects within the sample. These corrections can

be made, but there is much debate concerning their accuracy. Quite accurate quantitative analyses can be made when suitable standards similar in composition to the unknown are available. Most of the analyses done on the present instrument, however, have been of a qualitative nature, since these analyses are usually sufficient to solve most of the problems encountered. The following discussions illustrate how the electron probe has been used to solve various material problems encountered at GSFC during the past 2 years. These discussions are primarily concerned with the results of the electron probe examinations. Detailed descriptions of the tests and results can be found by consulting the appropriate references.

## THERMOELECTRIC BONDING STUDIES

A major source of degradation encountered with lead telluride (PbTe) thermoelectric elements can be traced to problems associated with the bond between the thermoelectric element and its end shoe, the end shoe being used to transmit the electrical power from the element to the load. The electron probe was used to study some of the characteristics of a SnTe - 1% Ti, braze bond joining a PbTe thermoelectric element to an iron shoe. These thermoelectric elements have potential use in radioactive isotope thermoelectric generators intended for use on future space probes as power sources. Examination was performed on "as-bonded" specimens as well as on specimens run at operating temperature for various periods of time (Reference 2). The purpose of the examination was to determine the distribution of the various elements before and after testing.

A photomicrograph of an as-bonded specimen, Figure 2, shows an area of the braze zone which connects the iron shoe on the left to the PbTe on the right. Metallographic examination revealed a series of spheroidal particles running parallel to the braze zone at the SnTe-PbTe interface.



Fe      →      ←      PbTe  
                  SnTe  
                  BRAZE  
                  ZONE

Figure 2—Photomicrograph (280X) of the braze zone between an iron shoe and PbTe thermoelectric element.

An Fe  $K\alpha$  X-ray scan, Figure 3, shows that the series of particles along the SnTe-PbTe interface is primarily iron. Superimposed on this photograph is a line profile trace of Fe  $K\alpha$

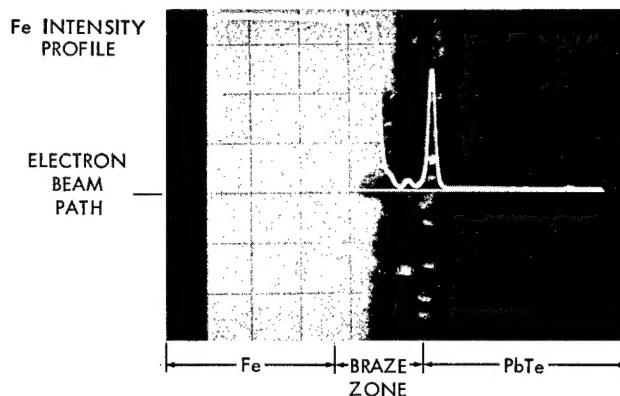


Figure 3—Fe $K\alpha$  X-ray scan of Fe-SnTe-PbTe interface in "as brazed" condition; Fe $K\alpha$  line superimposed on photograph; note inhomogeneous distribution of iron across braze zone; horizontal scale = 40 $\mu$  per division.

radiation. The horizontal line represents the path of the electron beam across the specimen. The intensity profile of the iron is artificially displaced from this path for clarity. It is apparent that the iron content which was initially 100 percent iron within the shoe drops almost to zero through the SnTe braze zone and increases dramatically as the electron beam traverses one of the particles at the SnTe-PbTe interface. There is a sharp cutoff of the iron intensity as the beam enters the bulk PbTe, indicating little or no diffusion of iron into the PbTe semiconductor at this point. This is in marked contrast to tin, which diffuses into the PbTe to a depth of approximately 35 microns, as can be observed in Figure 4. The diffusion of tin into the PbTe is indicated by the gradual reduction in the tin intensity as the electron beam enters the PbTe.

A specimen similarly brazed but operated at 900°F for 500 hours is shown in Figure 5. The backscatter presentation has superimposed upon it the line profile traces of iron, lead, and tin.

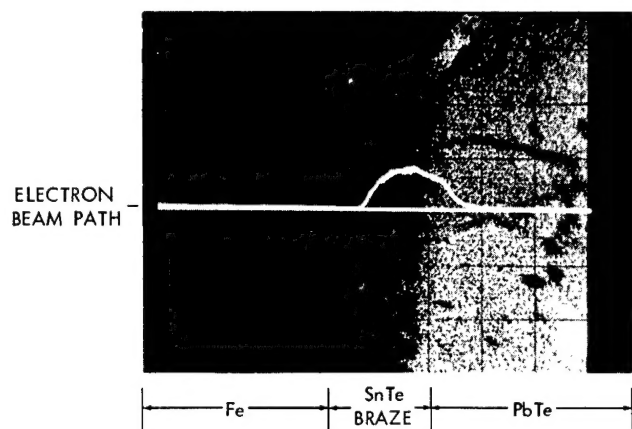


Figure 4—Backscatter electron image with superimposed SnLa line profile image (as brazed condition); note diffusion of tin into PbTe; horizontal scale = 40 $\mu$  per division.

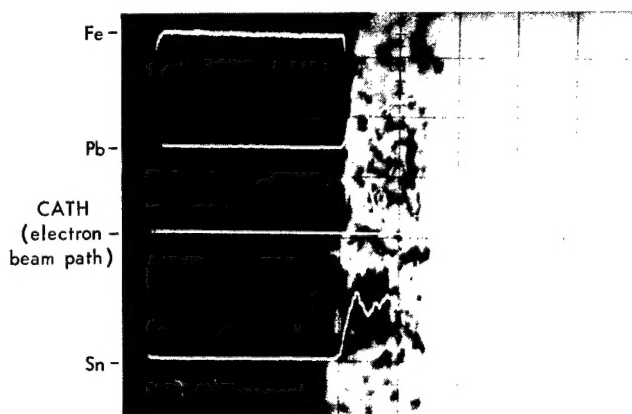


Figure 5—Backscatter electron image of 900°F, 500-hour test specimen with superimposed Fe, Sn, and Pb line profiles; note diffusion of Pb into SnTe braze and Sn into PbTe; horizontal scale = 40 $\mu$  per division.

Again, iron is distributed inhomogeneously throughout the braze zone as was observed in the as-bonded braze condition (Figure 3). Also,

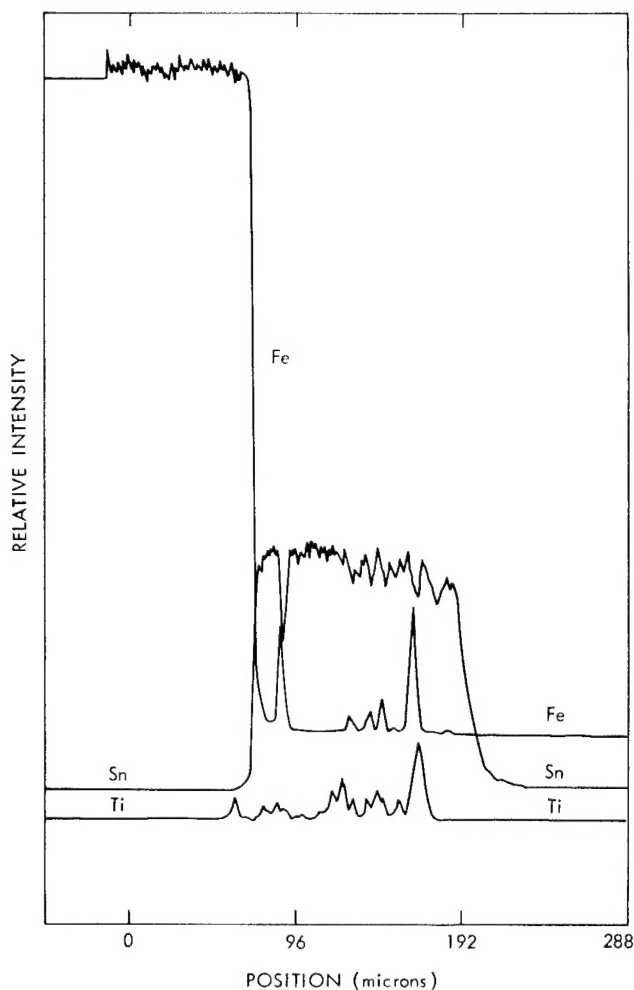


Figure 6—Intensity of Fe, Ti, and Sn versus position for as brazed specimen.



lead is distributed throughout the braze zone indicating considerable diffusion of this element from the PbTe to the SnTe. The extensive diffusion of tin into the PbTe (up to 190 microns) is quite obvious.

Figures 6 and 7 show the intensities of iron, titanium, and tin plotted against position across the bond. Figure 6 is a plot of a PbTe-Fe couple in the brazed condition; the iron is still distributed inhomogeneously across the braze zone and appears to peak at the SnTe-PbTe interface. The titanium appears to be associated with particles of iron since the titanium and iron peaks generally coincide. The tin on the other hand, remains uniform across the braze zone and drops sharply at the PbTe-SnTe interface. Figure 7 is an intensity-position plot of a specimen which was run at 900°F for 5904 hours. Again, it can be seen that the iron and titanium coincide and are again distributed inhomogeneously throughout the braze zone. The tin, however, shows a diffusion gradient, a gradual reduction across the braze zone, with considerable intensity evident up to 240 microns into the PbTe. It is believed that the diffusion of tin is one of the factors leading to the degradation in the power output of some PbTe thermoelectric elements.

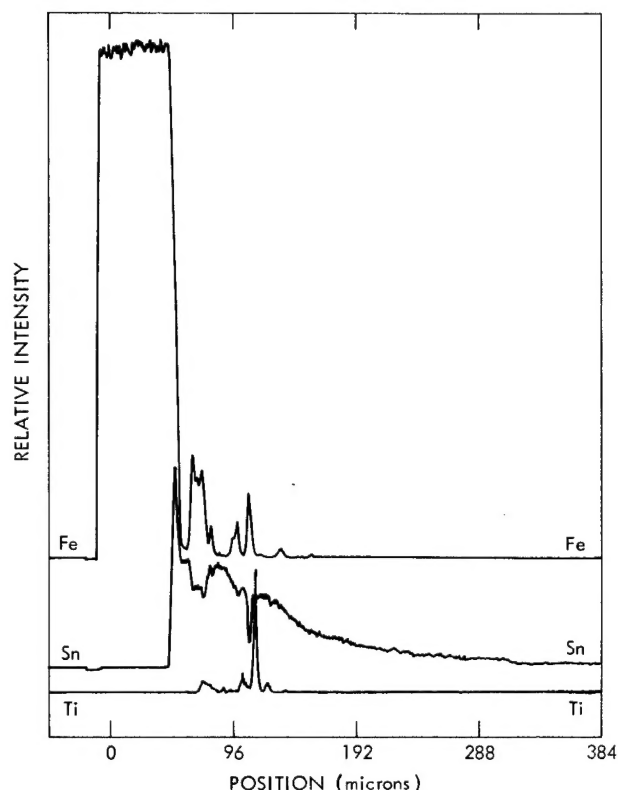


Figure 7—Intensity of Fe, Ti, and Sn versus position for 900°F, 5904-hour test specimen.

## PbTe-W DIFFUSION BOND

An electron probe analysis was performed on a lead telluride-to-tungsten diffusion bond. The PbTe-W bond was produced quite accidentally during a PbTe bonding study (Reference 3). Since this bond was discovered, additional effort has been expended to explain its nature. Bates et al. (Reference 4) have shown that PbTe and tungsten do not react at temperatures even up to the melting point of PbTe. Nevertheless, some type of bond between PbTe and W is formed.

Figure 8 shows an intensity profile trace of W-L $\alpha$ , Pb-L $\alpha$ , and Te-L $\alpha$  X-rays versus position which was made across the bond interface. There is an indication of definite diffusion of tungsten into the PbTe element to a distance of approximately 4 microns. It is also evident that there are no intermediate compounds formed between W, Pb, or Te in the bond zone. This confirms the results of Bates et al.; that is, there is no reaction between the tungsten and the PbTe. Since a strong bond is formed, it is obvious that something other than a PbTe-W reaction takes place. It is theorized that oxygen in the PbTe may take part in the bond reaction, or that dopants in the PbTe may react.

## SiGe-W DIFFUSION BOND

An analysis was performed on a SiGe thermoelectric diffusion-bonded to a tungsten shoe. The specimen was prepared during an investigation of segmented thermoelectric devices. The preparation and properties of the SiGe-W bonded specimen is discussed in a report by Bates and Weinstein (Reference 5).

A line profile analysis of the bond was performed. Figure 9 shows the intensities of Si-K $\alpha$ , Ge-K $\alpha$ , and W-L $\alpha$  X-rays plotted against electron beam position as the bond was traversed. It is evident that the bond is formed by a reaction between tungsten and silicon with the formation of a W-Si compound, as shown by the constant intensity level exhibited by tungsten and silicon in the bond zone. It is also apparent that in order for the reaction zone to form, extensive diffusion of silicon from the bulk SiGe occurs, as shown by the drop in the silicon intensity starting approximately 32 microns from the W-SiGe interface. At the same time, the germanium intensity begins to rise, peaking at the W-SiGe bond interface, the point where the silicon is at its lowest point. The increase in the germanium intensity results from the depletion of silicon and not from the diffusion of germanium into this area.

Backscatter electron and X-ray scan images were also made of the bond zone. These images, shown in Figure 10, substantiate the results obtained by the line profile analysis.

The backscatter electron presentation, Figure 10a, shows the bond zone quite clearly. The picture is biased electronically toward the heavier elements; therefore, the SiGe, whose average atomic number is less than that of tungsten, does not show up. Figure 10b-10d are W-L $\alpha$ , Si-K $\alpha$ , and Ge-L $\alpha$  X-ray scans of the same areas as shown in 10a. Note the presence of silicon and tungsten and the absence of germanium in the bond zone. Also, note the area on the SiGe side of the bond zone (Figure 10c) which is depleted in silicon.

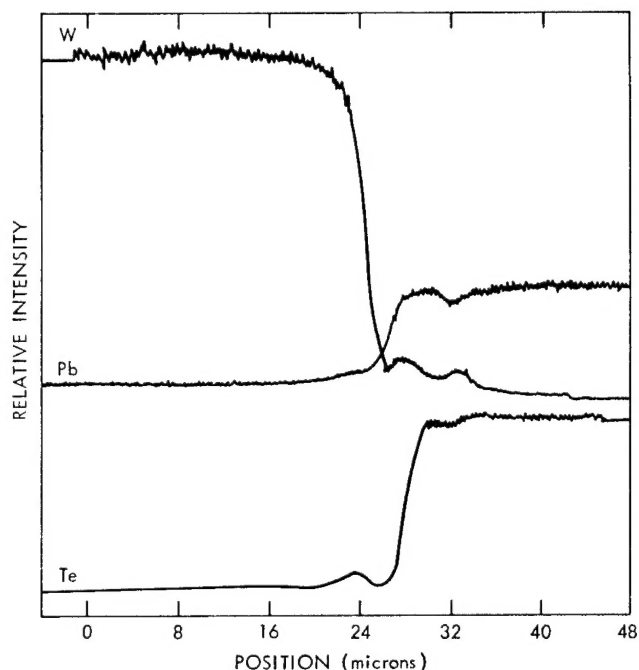


Figure 8—Intensity profile trace of W-L $\alpha$ , Pb-L $\alpha$ , and Te-L $\alpha$  X-rays versus position across bond interface.

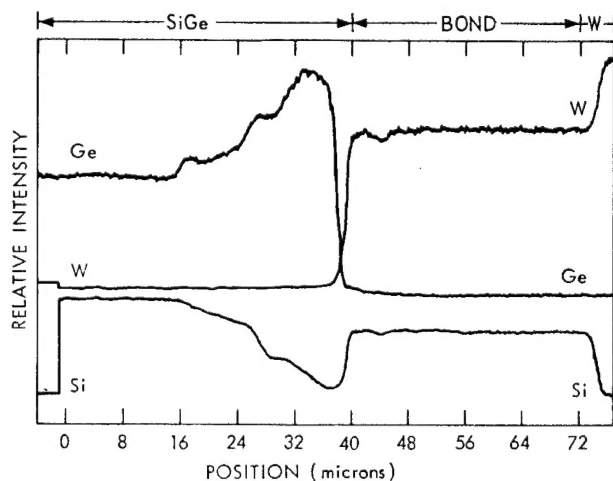


Figure 9—Intensity profile trace of Si-K $\alpha$ , Ge-K $\alpha$ , and W-L $\alpha$  X-rays versus electron beam position.

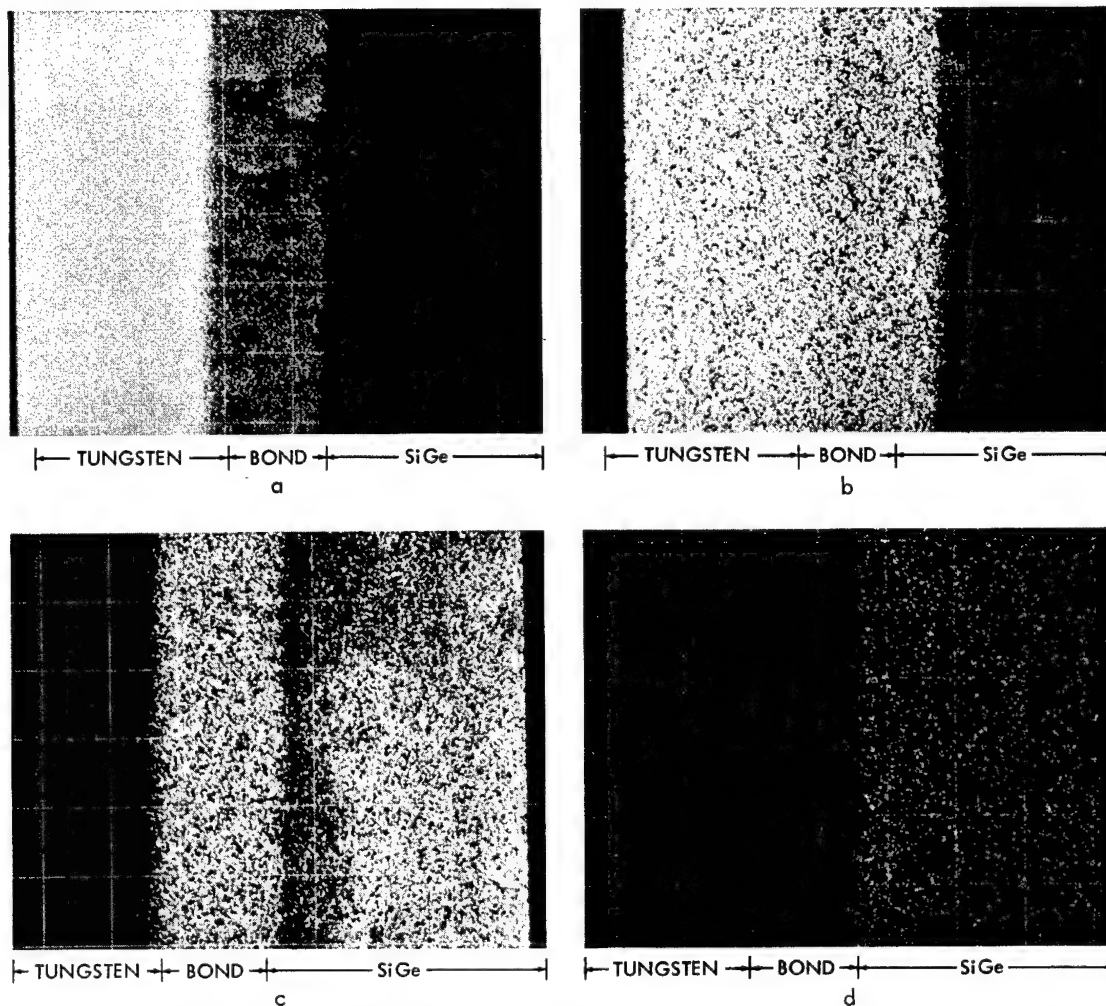


Figure 10—SiGe-W diffusion-bonded element; (a) backscatter electron image biased to heavy elements; horizontal scale =  $10\mu$  per division; (b) tungsten  $L\alpha$  X-ray scan, same area as (a); (c) silicon  $K\alpha$  X-ray scan, same area as (a) showing depletion of silicon on SiGe side of bond zone; (d) germanium  $K\alpha$  scan, same area as (a).

## STRENGTHENING OF PbTe

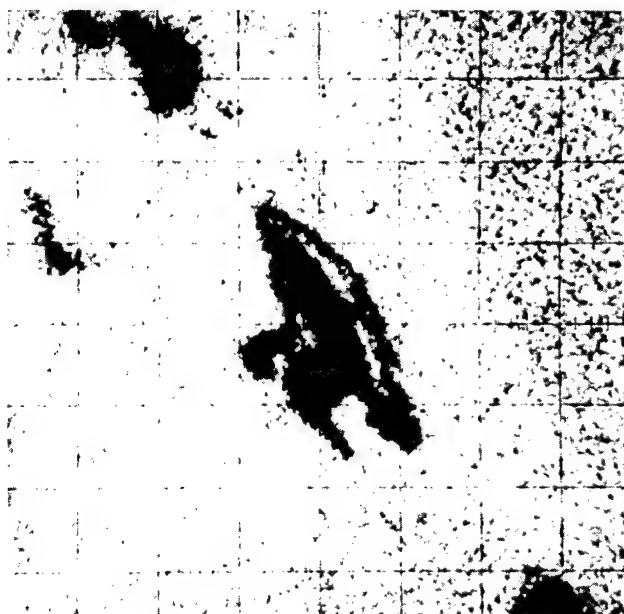
During the bonding study of PbTe previously referred to, some effort was made to strengthen PbTe without degrading the electrical properties of the couples. One method consisted of adding 1 percent molybdenum fibers to the PbTe powder prior to hot pressing (Reference 6). The elements were then bonded to the iron shoes as before and tested for various lengths of time at operating temperatures. Metallographic examination of the samples containing the molybdenum wire clearly shows a reaction zone around the individual wires. This reaction zone was observed in areas near the hot side of the tested elements as well as in areas near the cold side. Electron probe examination was performed in order to determine the nature of the reaction. Figure 11a shows a backscatter electron image of a molybdenum wire approximately 170 microns from the cold side braze zone. Figure 11b is a  $MoL\alpha$  X-ray scan of the same area which shows some



a



b



c



d

Figure 11—Specimen of PbTe containing molybdenum wire,  $170\mu$  from cold side of braze zone; horizontal scale =  $40\mu$  per division; (a) backscatter electron image; (b) Mo- $L\alpha$  X-ray scan showing diffusion of Mo into PbTe matrix; (c) Te- $L\alpha$  X-ray scan; compare with (b) and note presence of Te in same area as Mo; (d) Fe- $K\alpha$  X-ray scan showing concentration of iron in reaction zone around Mo wire.

diffusion of molybdenum into the PbTe matrix. A tellurium X-ray scan, Figure 11c, shows the presence of tellurium in the same areas as was observed with molybdenum. In addition, the area around the wire appears to act as a sink for iron since, even 170 microns from the PbTe-SnTe interface, considerable iron was observed. This situation is shown in Figure 11d, which is a FeK $\alpha$  X-ray scan of the same areas as Figure 11a. Notice that iron, tellurium, and molybdenum are concentrated in the reaction zone. No diffusion of iron or tellurium into the molybdenum wire was observed, however. Similar results were observed during an examination of wire near the hot-side braze zone. These results are shown in Figures 12a through 12d. Figure 12a is a backscatter electron image with a line profile trace of molybdenum and tellurium superimposed upon it. Molybdenum increases in intensity at point A outside of the wire itself, and the intensity of tellurium increases sharply at the same point, indicating a concentration of tellurium there (the path of the electron beam is indicated by the horizontal line across the center of the picture). The intensity profiles are artificially displaced from this line for clarity. It is apparent that the reaction zone forms at a fairly low temperature (400°F), although at higher temperatures the reaction zone is more distinctive (compare Figure 12 with Figure 11). For wires that were far removed from the bond zone, there was no evidence of iron in the reaction zone; however, tellurium and molybdenum do continue to react. The strengthening effect noted by the addition of the molybdenum wire to the PbTe is believed to be caused by the removal of excess tellurium from the matrix (Reference 6); however, long-term tests have not been performed, and it is not known how the electrical properties are affected by this addition.

## FAILURE ANALYSIS OF H<sub>2</sub>O<sub>2</sub> STORAGE BOTTLE

A problem arose involving the leakage of H<sub>2</sub>O<sub>2</sub> from storage bottles which were to be located on the Syncom, Early Bird, and Applications Technology Satellites (Reference 7). The storage bottles and fittings were fabricated from 1060 aluminum with a 99.6 percent purity and were given a passivation treatment with nitric acid prior to filling. To test a completed system, the bottles were charged with 90 percent H<sub>2</sub>O<sub>2</sub> while the pressure was monitored. In some tests, leakage occurred in fittings which were machined from extruded 1-1/2-inch bar stock. Metallographic examination of these fittings revealed elongated inclusions, but these were shown to be not responsible for the observed leakage. An electron probe examination was then performed to determine the cause of the failures.

A plot of intensity versus probe position was made across an area extending from the tip of a corrosion pit toward the bulk metal. A schematic representation of the area of analysis is shown in Figure 13. A typical analysis of 1060 aluminum gives the following composition (Reference 8): 99.6 percent Al, 0.25 percent Si maximum, 0.35 percent Fe maximum, and 0.05 percent Cu maximum, with smaller amounts of Mn, Ti, Mg, Zn; therefore a scan for iron, silicon, and copper, the major impurities, was performed. Scans were made over a distance of 288 microns, which covered the width of the corrosion pit at its widest point. Six scans, 100 microns apart, were made. Analysis revealed a constant, low level of copper and silicon. The iron content, however, shown in Figure 14, revealed a very inhomogeneous distribution ranging from concentrations approximating

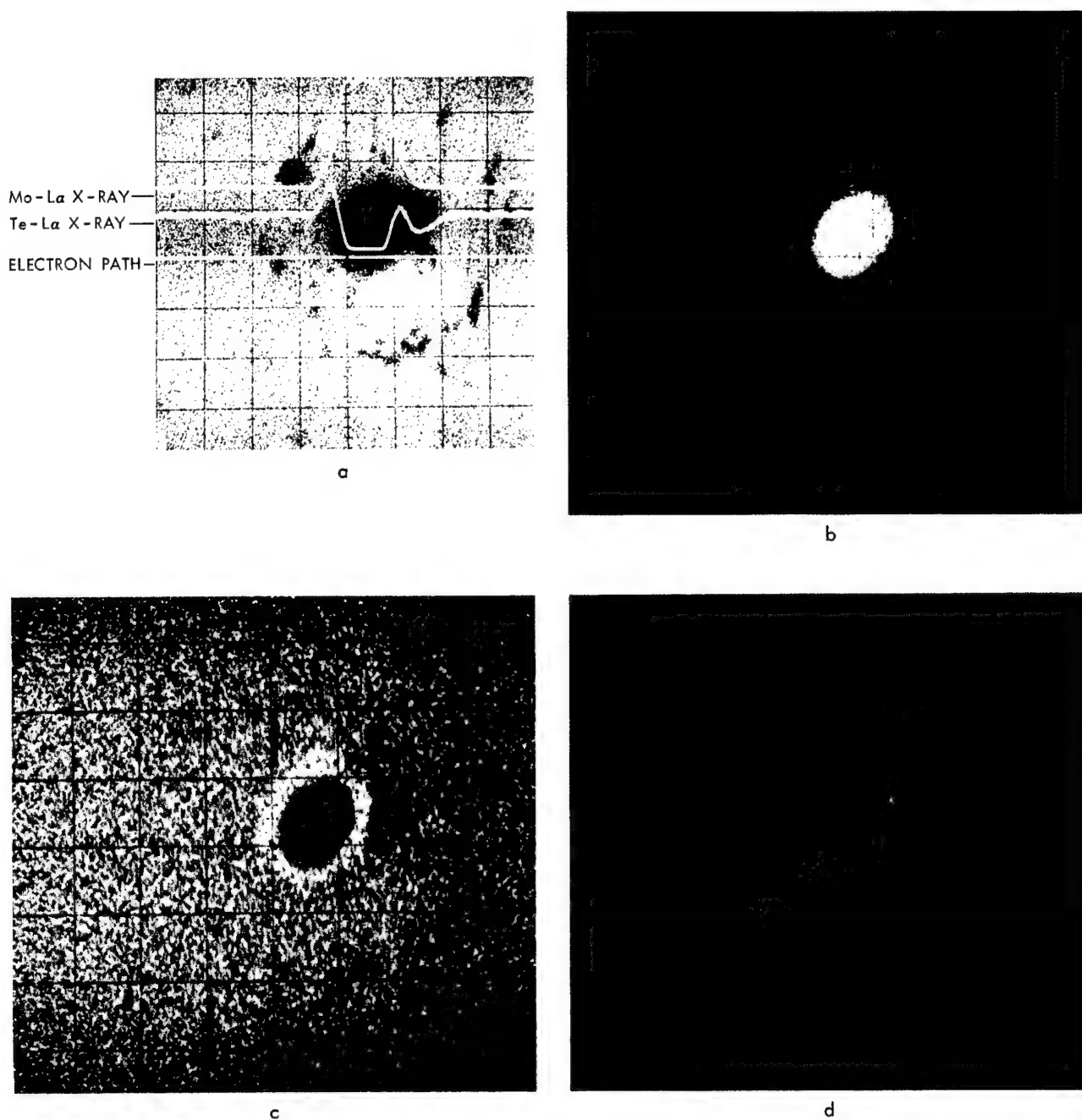


Figure 12—Specimen of PbTe containing molybdenum wire, near hot side of braze zone; horizontal scale =  $20\mu$  per division; (a) backscatter electron image with superimposed line profile traces of Mo-L $\alpha$ , and Te-L $\alpha$  X-ray intensities; (b) Mo-L $\alpha$  X-ray scan showing diffusion of Mo into PbTe matrix; (c) Te-L $\alpha$  X-ray scan showing concentration of Te around wire; (d) Fe-K $\alpha$  X-ray scan showing Fe concentration in reaction zone around Mo wire.

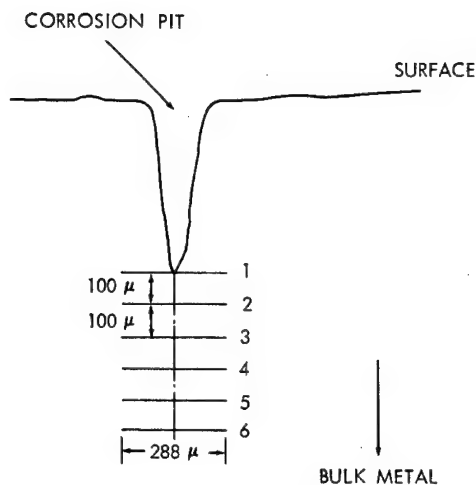


Figure 13—Schematic representation of analysis area of 1060 aluminum containing corrosion pits.

the typical analysis content to amounts containing as much as 35 percent iron. It can be seen that the peak iron concentrations generally lie inline with one another within the area scanned. An iron  $K\alpha$  X-ray scan near the end of one of the corrosion pits was made and is shown in Figure 15. The inhomogeneous distribution of iron is plainly evident. It is believed that the iron in these areas was attacked by the nitric acid during passivation, causing the corrosion pits which are the most likely path for leakage of the  $H_2O_2$ .

The problem was solved by annealing the material at 1100°F for 16 hours. This treatment resulted in a more homogeneous distribution of iron and thereby prevented the formation of corrosion pits.

## ALLOY DEVELOPMENT

### Ruthenium vs Zinc Reactions

Zinc has been proposed as a coating on columbium metal for oxidation protection at high

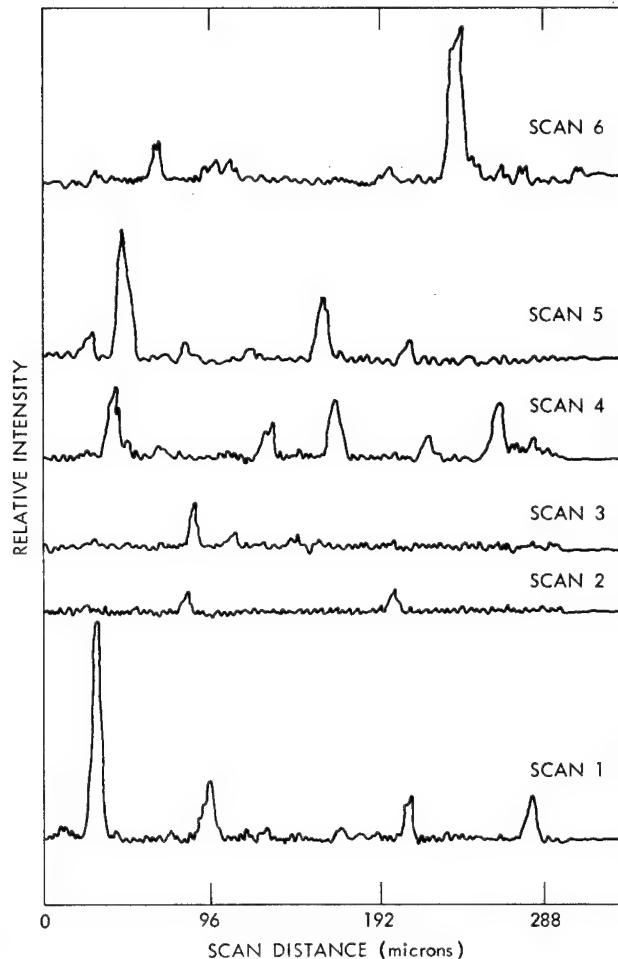


Figure 14—Fe intensity versus probe position over analysis area of 1060 aluminum containing corrosion pits; six scans, 100  $\mu$  apart, are shown.

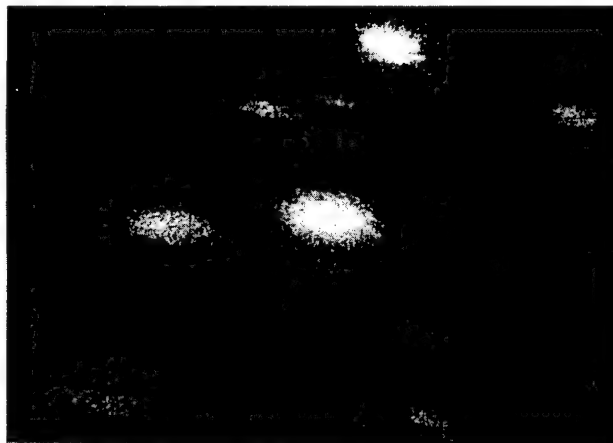
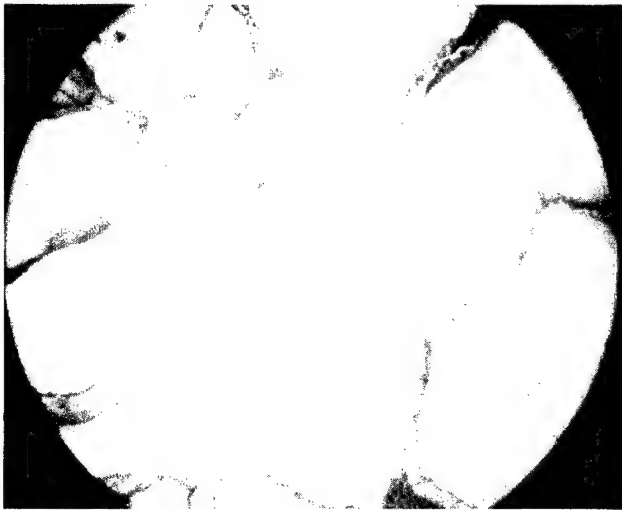
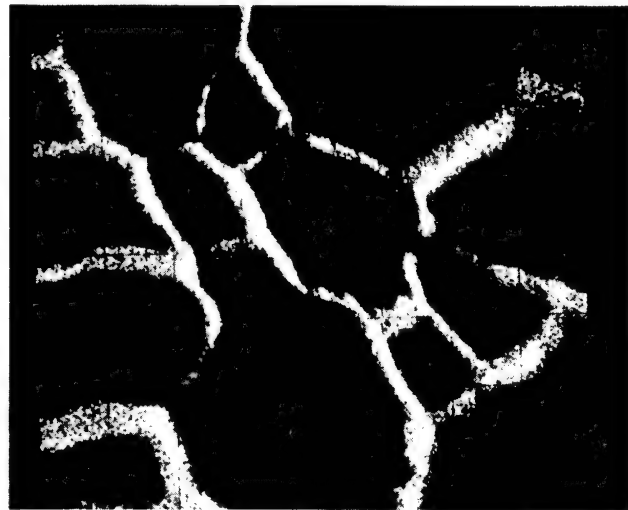


Figure 15—Fe- $K\alpha$  X-ray scan of 1060 aluminum near tip of corrosion pit; horizontal scale = 5  $\mu$  per division.

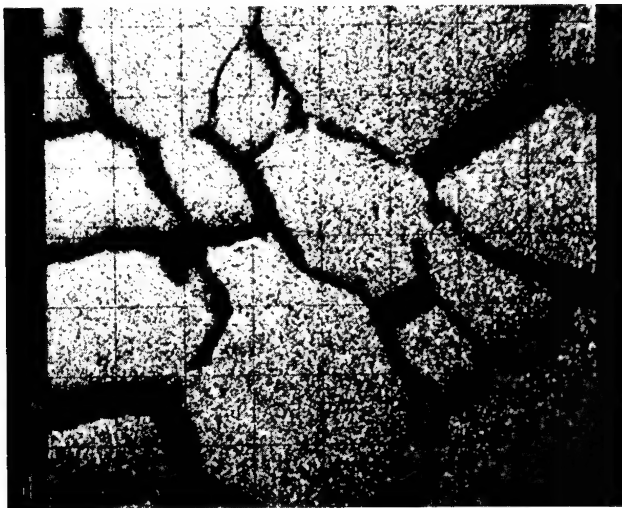
temperatures (Reference 9). A study was undertaken at GSFC to determine if a similar protective reaction occurred with ruthenium and rhodium. In the first test, ruthenium and zinc were placed together in a reaction vessel, which was then evacuated. The specimen was heated to 450°C for 100 hours. This temperature is well above the melting point of zinc, but below that of ruthenium. After being cooled, the material was cut and polished for metallographic examination. This examination revealed large grains which were surrounded by a second phase isolated in the grain boundaries, Figure 16a. Electron probe examination, Figures 16b and 16c, revealed that the grain boundary phase was almost entirely zinc, whereas the grains were essentially ruthenium. It was obvious that the molten zinc attacked the ruthenium intergranularly but did not penetrate the grains to any extent. Therefore, zinc would not be recommended as a protective coating for ruthenium since an extensive corrosive reaction occurs between the two metals.



a



b



c

Figure 16—Analysis of ruthenium-zinc system; (a) photomicrograph (250X) showing intergranular phase; (b) Zn-K $\alpha$  X-ray scan of same area, horizontal scale = 40  $\mu$  per division; (c) Ru-L $\alpha$  X-ray scan of same area and same scale.



## Rhodium-Zinc

A similar test was performed on a rhodium-zinc system because rhodium is chemically related to ruthenium and also has a high melting point. Metallographic examination of the post-test materials, Figure 17a, showed two distinct areas. One area was obviously rhodium which did not melt at the heat treatment temperature and which still retained its original shape. The

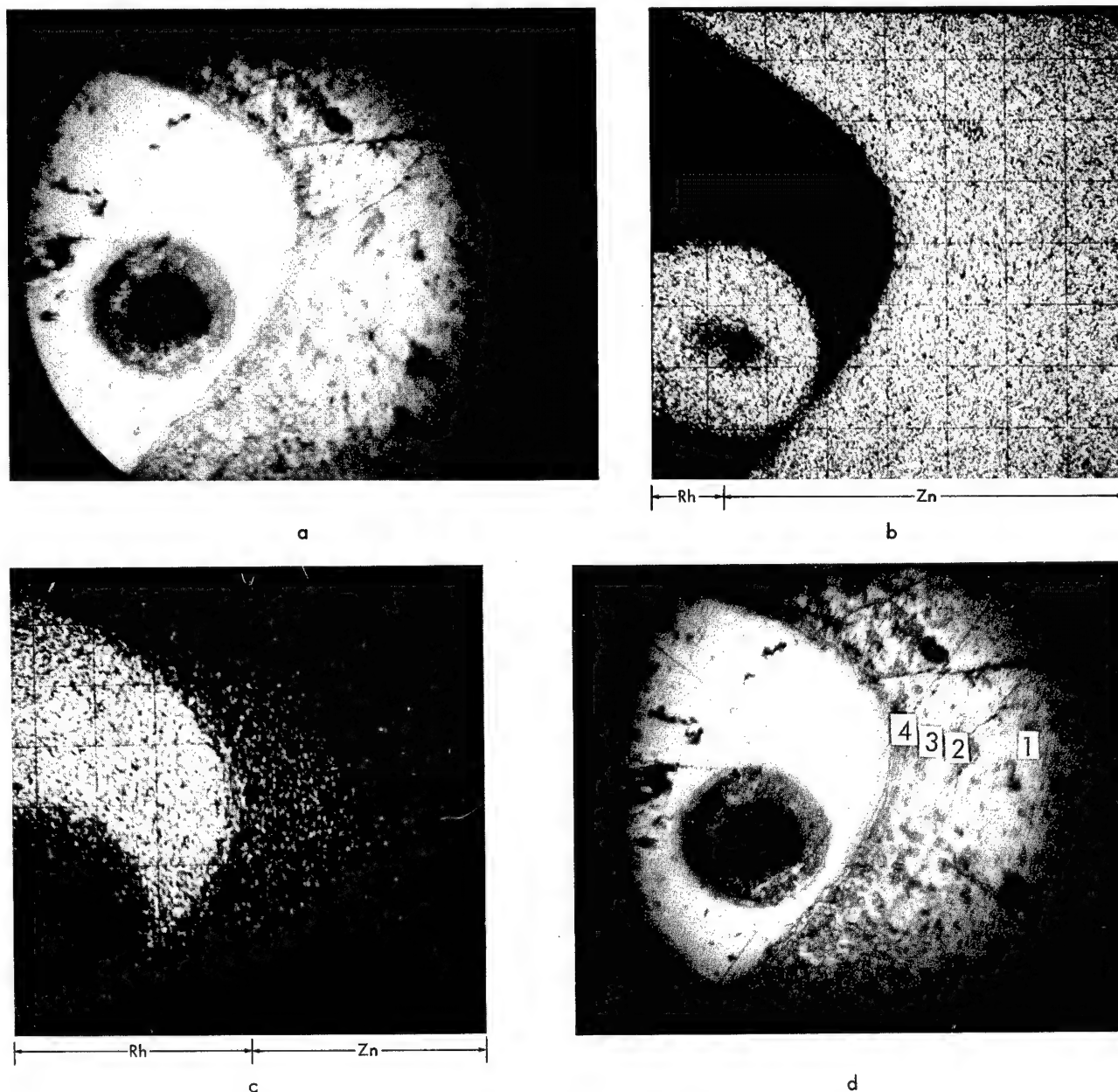


Figure 17—Analysis of rhodium-zinc system; (a) photomicrograph (250X); (b) Zn-K $\alpha$  X-ray scan of same area, showing absence of appreciable zinc in Rh zone; horizontal scale = 40  $\mu$  per division; (c) Rh-L $\alpha$  X-ray scan of same area, showing diffusion of Rh into Zn area; (d) photomicrograph (250X) showing zones in the Zn matrix which were quantitatively analyzed for Zn.

other area was apparently zinc which had melted and solidified. Electron probe examination, Figure 17b, which is a zinc  $K\alpha$  X-ray scan of the area shown in Figure 17a, showed a sharp separation between the two areas with little or no diffusion of zinc into the rhodium. The circular concentration of zinc in the rhodium is believed to have resulted from a hole in the rhodium into which the molten zinc flowed during the heat treatment. Figure 17c, the rhodium X-ray scan, shows an apparent diffusion of rhodium into the zinc. A semi-quantitative analysis of this apparent diffusion zone was made at a different distance from the interface, outward as shown in Figure 17d. The intensity ratios  $I/I_0$  for zinc uncorrected for absorption effects are as follows:

<u>Position</u>	<u>% Zn</u>	<u>% Rh (by difference)</u>
Zn matrix (1)	83.2	16.9
Zone (2)	61.4	38.6
Zone (3)	41.3	58.7
Zone (4)	2.2	97.8

These results together with the X-ray scans indicated the possible existence of three inter-metallic compounds formed between rhodium and zinc. The  $Rh_5Zn_{21}$  compound (72.74 wt. % Zn) had been reported in the scientific literature, but this particular composition is not evident in the data reported here.

### **Rhenium Alloys**

Unalloyed rhenium filaments intended for use in satellite mass spectrometers have shown unexpected failure during testing. In an attempt to overcome this problem, methods of strengthening the filaments by the addition of refractory compounds have been explored (Reference 10). Various refractory carbides, nitrides, and borides in powder form were mixed with rhenium powder. The mixed powders were then hand-pressed into pellets and heated and/or melted in a hollow cathode furnace. Following the treatment in the furnace, the resultant pellets were examined metallographically and then with the electron probe. Probe analysis was performed in order to detect variations in concentration that occur among the various elements, as in the case of the formation of intermetallic compounds. Typical of the specimens examined is that of Re-WC. Figure 18a shows a backscatter electron presentation of rhenium-tungsten carbide particles. However, in specimens that had been melted rather than just heat-treated, no such concentration of carbides was observed. Instead, a rather uniformly distributed second phase was observed with the probe. The analysis indicates that the carbide decomposes and becomes uniformly dispersed when reacting during the melting of the specimens.

### **Magnesium-Yttrium-Aluminum Alloys**

Studies have been underway to increase the strength and temperature capabilities of magnesium alloys by the addition of a suitable third component. One of the selected additive elements is yttrium. Various Mg-Y-Al alloy compositions have been made, and additional studies to optimize

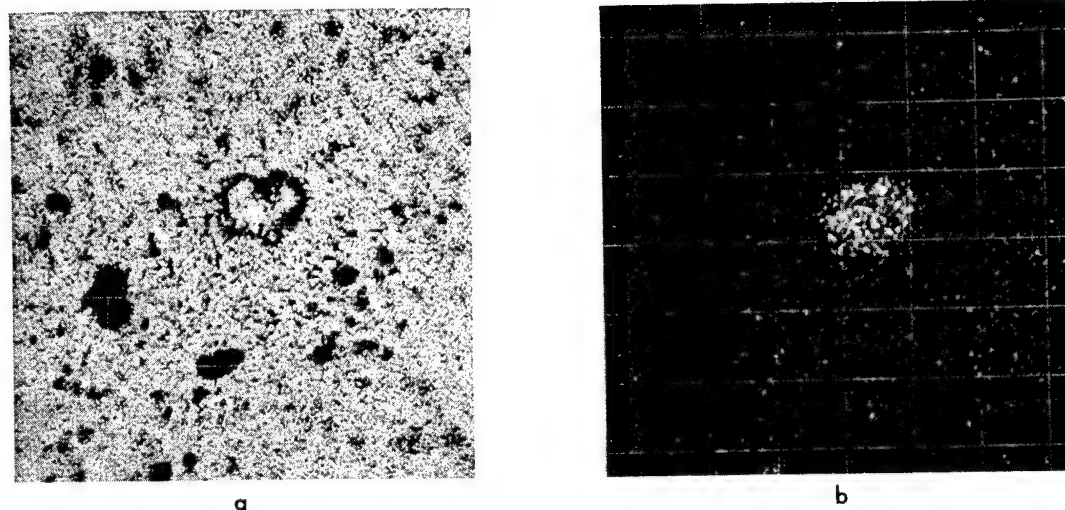


Figure 18—Results of electron probe microanalysis of rhenium-tungsten carbide heated to 2000°C:  
(a) backscatter electron image; (b) tungsten X-ray emission.

the alloy composition are continuing. The alloys were made in an inert atmosphere in a carbon crucible, utilizing an induction furnace for heating. The alloys were prepared by premelting each of the components from bar stock and then remelting them several times for homogeneity. Some magnesium was lost because of its low vapor pressure, but these losses were made up before each remelt.

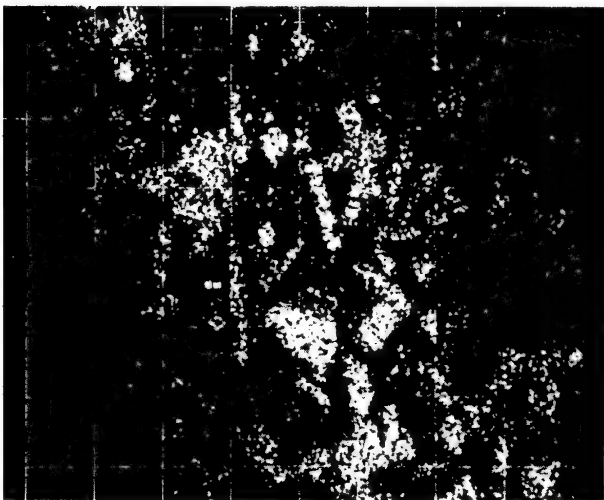
Metallographic examination of a Mg-8Y-1.9Al alloy is shown in Figure 19a. It can be observed that there is a two-phase field with one phase consisting of highly discrete, massive particles surrounded by a uniformly distributed, second-phase matrix. Electron probe examination was performed to determine the compositions of these phases. Figure 19b shows a backscatter electron image of a Mg-8Y-1.9Al specimen. Notice that the particles are brighter than the matrix, indicating a material of heavier atomic number than the matrix. Figures 19c, 19d, and 19e are Y-L $\alpha$ , Al-K $\alpha$ , and Mg-K $\alpha$  X-ray scans of the specimen. It is readily seen that the particles are primarily an yttrium-aluminum compound, whereas the matrix is primarily magnesium. Semiquantitative analysis verifies these results, indicating that the major constituents of the particles are yttrium and aluminum, with only 1.3 percent aluminum in the magnesium matrix. There is also some indication that the Y-Al particles contain some carbon and oxygen although the amounts present are less than 1 percent. Similar results were obtained with a Mg-2Y-7.9Al alloy. The intermetallic particles in this sample appeared to have approximately the same amount of aluminum and yttrium as the first sample, and it was obvious that a Y-Al compound was formed just as in the first rather than a homogeneous solution of yttrium and aluminum in magnesium. The presence of the Y-Al intermetallic compound corresponds quite well to that of the Y-Al compounds described in the phase diagram given by Elliott (Reference 11). It is obvious that yttrium and aluminum are combining during the melting, preventing the complete solution of these compounds in the alloy. Since the Y-Al intermetallic compound is an inherent part of the system, efforts are being formulated to use this as a strengthening agent in the alloy. To do this, the intermetallic must be made much smaller in size and should be distributed more homogeneously within the alloy. One method to accomplish this is to formulate the alloy from powder products. This method is being contemplated for future work.



a



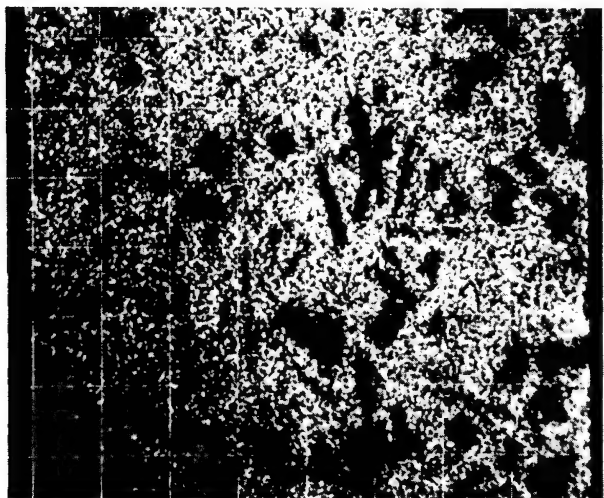
b



c



d



e

Figure 19—Section of Mg-8Y-1.9Al alloy: (a) photomicrograph (400X); (b) backscatter electron image, horizontal scale =  $40\mu$  per division; (c) yttrium  $L\alpha$  X-ray scan of same area; (d) aluminum  $K\alpha$  X-ray scan of same area; (e) magnesium  $K\alpha$  X-ray scan of same area.

## FRICTION AND WEAR

A study is currently underway to determine the wear and frictional behavior of coated and uncoated metal surfaces. This study relates the metallurgical and mechanical property changes brought about in material as a result of frictional action under simulated space environments. During these tests, rider material is rubbed against a plate material (which may be the same or a different material) at a constant speed either in air or in a vacuum. The changing force generated by friction between the two materials is monitored, and metallurgical examination of both the rider

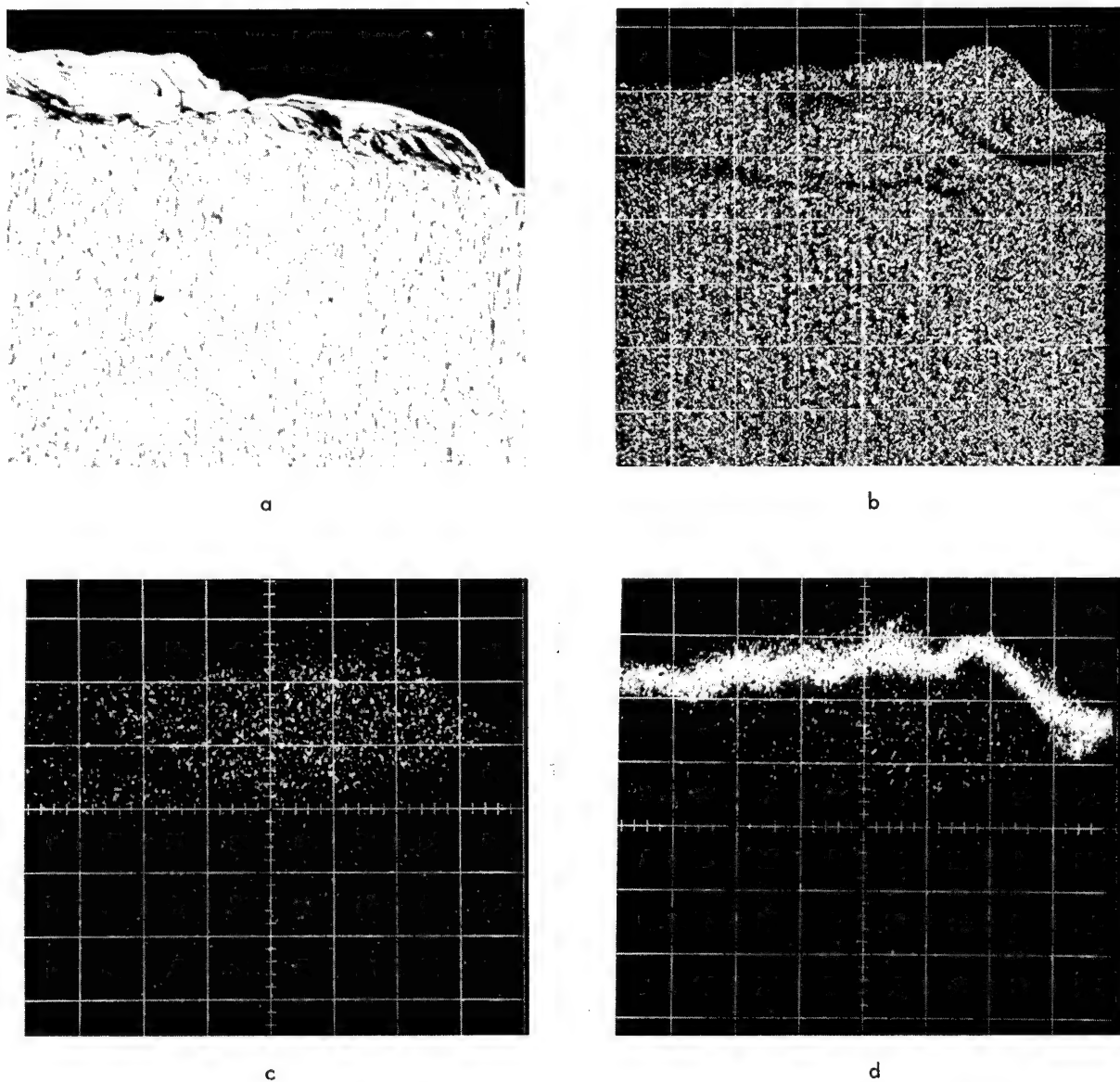


Figure 20—Portion of surface of a 1020 steel rider which had been rubbed against a 4320 steel plate: (a) photomicrograph (250X); (b) backscatter electron image; horizontal scale =  $40\mu$  per division; (c) chromium K $\alpha$  X-ray scan of same area; (d) nickel K $\alpha$  X-ray scan of same area, showing nickel plating on surface and in area coinciding with that of the chromium in (c).



Figure 23—Transverse crack in nonetched (a) and nital-etched (b) conditions at 500X to show tin in crack. The electron microprobe photograph (c) identifies tin. The scan does not fully reach the surface in this case to reveal the tin plating.



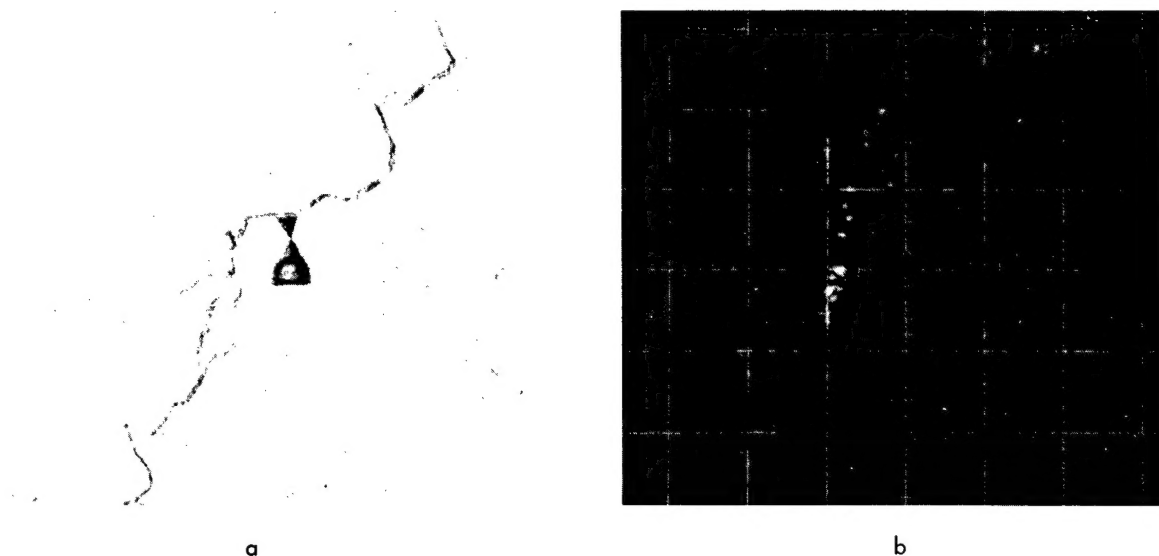


Figure 24—Terminal end of a transverse crack in the nonetched condition at 500X (a) and photograph (b) of tin X-ray which reveals presence of tin in the very tight extremity of the crack.

## FAILURE OF NIMBUS SEPARATION SPRINGS

A problem involving cracking of tin-plated separation springs intended for use on a Nimbus satellite was investigated with the probe (Reference 12). Metallographic examination of sections of the springs were made. Both transverse and longitudinal sections revealed that the steel was not unusually high in inclusion content and that the microstructure consisted of a fine, acicular, tempered martensite which appeared 100 percent transformed. This can be seen in Figure 22a. Figure 22b shows the surface end of one of the transverse cracks in the coil. The layer on the surface is the tin-plating referred to previously.

Examination of the crack at high magnification revealed the presence of tin, as shown in Figure 23a and 23b. An electron probe examination of the crack using a tin X-ray scan revealed the presence of tin in the crack (Figure 23c). Tin X-ray scans were also made at the tip of the crack to determine whether tin had penetrated to this point. An example of one of the crack tips is shown in Figure 24a; the tin X-ray scan is shown in Figure 24b, which shows tin penetration even to the crack tip.

It is believed that the throwing power of the tin-plating solution was not sufficient to deposit tin at the tip of an already existing crack. Therefore, the crack is believed to have resulted from intergranular penetration by the tin into the highly stressed steel during the hydrogen stress-relieving operation which was conducted after the tin was applied. On the basis of this analysis, Babecki and Jellison (Reference 12) concluded that on future springs of this design, a more effective stress relief be effectuated by a combination of higher temperature and longer times. Also they concluded that if tin plating is continued, care should be taken to insure that the melting point of tin is not attained during any step in the fabrication process.

## CONCLUDING COMMENT

Examples have been given to illustrate the versatility of the electron probe in metallurgical analysis and in finding solutions for specific materials engineering problems. These examples and many other applications of the probe have proved it to be a powerful tool in problems ranging from materials research to quick-reaction failure analyses.

Goddard Space Flight Center  
National Aeronautics and Space Administration  
Greenbelt, Maryland, 26 July 1967  
129-03-04-02-51

## REFERENCES

1. Castaing, R., "Application of Electron Probe to Local Chemical and Crystallographic Analysis," Thesis, University of Paris, June 8, 1951, Translation by California Institute of Technology, Pasadena, California, Dec. 1, 1955.
2. Eiss, A. L., "Thermoelectric Bonding Study Phase II Summary Report," Hittman Associates, NASA Contract NAS 5-3973, April 1966.
3. "Lead Telluride Non-Magnetic Bonding Research Study" First Interim Summary Report, February 26, 1965, to October 30, 1966, Tyco Laboratories, Inc., Bear Hill, Waltham, Mass., Contract No. NAS 5-9149.
4. Bates, H. E., Wald, F., and Weinstein, N., "The Bonding of Lead Telluride with Non-Magnetic Electrode," Proceedings IEEE/AIAA Thermoelectric Specialists Conference, Paper No. 15, May 17-19, 1966.
5. Bates, H. E., and Weinstein, M., "The Preparation and Properties of Segmented Lead Telluride-Silicon Germanium Thermoelements," Proceedings IEEE/AIAA Thermoelectric Specialists Conference, Paper No. 14, May 17-19, 1966.
6. Eiss, A. L., "Studies of Lead Telluride Thermoelectric Elements," Proceedings IEEE/AIAA Thermoelectric Specialist Conference, Paper No. 2, May 17-19, 1966.
7. Babecki, A. J., Grimsley, J. D., and Frankel, H. E., "An Analysis of Failures in Spacecraft," *Metal Progress* 91(2), February 1967.
8. "Metals Handbook," Vol. 1, 8th Edition, Metals Park, Novelty, Ohio: American Society for Metals, 1961.



9. "Protecting Columbium with Zinc," *Metal Progress* 81; 172-175, March 1962.
10. Park, J. J., Hasson, D. M., and Morely, J. R., "Strengthening of Rhenium with Refractory Carbides Using Hollow Cathode Melting," National Metals Congress, American Society for Metals, 1966.
11. Elliott, P. R., "Composition of Binary Alloys, First Supplement," New York: McGraw-Hill Book Company, 1965, p. 64.
12. Babecki, A. J., and Jellison, J., Internal Memo, "Investigation of Nimbus Separation Springs," May 3, 1967.

NATIONAL AERONAUTICS AND SPACE ADMINISTRATION  
WASHINGTON, D. C. 20546  
OFFICIAL BUSINESS

  
FIRST CLASS MAIL

POSTAGE AND FEES PAID  
NATIONAL AERONAUTICS AND  
SPACE ADMINISTRATION

06U 001 40 55 4ES 69046 68168 01195  
BATTELLE MEMORIAL INSTITUTE  
DEFENSE METALS INFORMATION CENTER  
COLUMBUS LABORATORIES  
505 KING AVE.  
COLUMBUS, OHIO 43201  
ATT ROGER J. RUNCK

POSTMASTER: If Undeliverable (Section 158  
Postal Manual) Do Not Return

*"The aeronautical and space activities of the United States shall be conducted so as to contribute . . . to the expansion of human knowledge of phenomena in the atmosphere and space. The Administration shall provide for the widest practicable and appropriate dissemination of information concerning its activities and the results thereof."*

— NATIONAL AERONAUTICS AND SPACE ACT OF 1958

## NASA SCIENTIFIC AND TECHNICAL PUBLICATIONS

**TECHNICAL REPORTS:** Scientific and technical information considered important, complete, and a lasting contribution to existing knowledge.

**TECHNICAL NOTES:** Information less broad in scope but nevertheless of importance as a contribution to existing knowledge.

**TECHNICAL MEMORANDUMS:**  
Information receiving limited distribution because of preliminary data, security classification, or other reasons.

**CONTRACTOR REPORTS:** Scientific and technical information generated under a NASA contract or grant and considered an important contribution to existing knowledge.

**TECHNICAL TRANSLATIONS:** Information published in a foreign language considered to merit NASA distribution in English.

**SPECIAL PUBLICATIONS:** Information derived from or of value to NASA activities. Publications include conference proceedings, monographs, data compilations, handbooks, sourcebooks, and special bibliographies.

**TECHNOLOGY UTILIZATION PUBLICATIONS:** Information on technology used by NASA that may be of particular interest in commercial and other non-aerospace applications. Publications include Tech Briefs, Technology Utilization Reports and Notes, and Technology Surveys.

*Details on the availability of these publications may be obtained from:*

SCIENTIFIC AND TECHNICAL INFORMATION DIVISION  
NATIONAL AERONAUTICS AND SPACE ADMINISTRATION  
Washington, D.C. 20546